CSIRO PUBLISHING

www.publish.csiro.au/journals/pasa *Publications of the Astronomical Society of Australia*, 2008, **25**, 105–113

A Pilot Survey for the H_2O Southern Galactic Plane Survey

Andrew J. Walsh[A,F]*, Nadia Lo*[B,C]*, Michael G. Burton*[B]*,*
Graeme L. White[A]*, Cormac R. Purcell*[D]*, Steven N. Longmore*[E]*,*
Chris J. Phillips[C]*, and Kate J. Brooks*[C]

[A] Centre for Astronomy, James Cook University, Townsville, QLD 4811, Australia
[B] School of Physics, University of NSW, Sydney, NSW 2052, Australia
[C] Australia Telescope National Facility, CSIRO, PO Box 76, Epping, NSW 1710, Australia
[D] Alan Turing Building, University of Manchester, Oxford Road, Manchester, M13 9PL, UK
[E] Harvard-Smithsonian Center for Astrophysics, 60, Garden Street,
Cambridge, MA 02138, USA
[F] Corresponding author. Email: andrew.walsh@jcu.edu.au

Received 2008 January 21, accepted 2008 March 25

Abstract: We describe observations with the Mopra radiotelescope designed to assess the feasibility of the H_2O Maser Southern Galactic Plane Survey. We mapped two one-square-degree regions along the Galactic plane using the new 12-mm receiver and the UNSW Mopra spectrometer. We covered the entire spectrum between 19.5 and 27.5 GHz using this setup with the main aim of finding out which spectral lines can be detected with a quick mapping survey. We report on detected emission from H_2O masers, NH_3 inversion transitions (1,1), (2,2) and (3,3), HC_3N (3–2), as well as several radio recombination lines.

Keywords: masers — surveys — stars: formation — ISM: molecules — Galaxy: structure

1 Introduction

The Mopra radio telescope is a 22-m single dish situated near Siding Spring mountain in New South Wales, Australia. Recent upgrades of the telescope included a new 12-mm receiver that operates in the frequency range of 16–27.5 GHz. In addition to this, the UNSW Mopra spectrometer (MOPS) allows instantaneous bandwidth coverage of over 8 GHz (most of the 12-mm band) sampled by 32 768 channels. Thus, MOPS potentially allows many spectral lines to be observed simultaneously. These new hardware, together with the on-the-fly mapping capability of the telescope, allow for very efficient multiple-line surveys of the southern sky.

Previous observations at 3 mm (Bains et al. 2006) have shown that the system works well over small regions, but it is the purpose of this work to test the system when mapping degree-scale regions of the Galaxy at 12 mm. Our ultimate aim is to map a large portion of the southern Galaxy in a survey we call 'HOPS' (the H_2O Plane Survey). The brightest spectral lines in this part of the spectrum are the H_2O (6_{16}–5_{23}) maser line at 22.235 GHz and NH_3 inversion transitions, which form the main focus of our survey. The 22.235 GHz H_2O masers are commonly found towards regions of both low and high mass star formation (Genzel & Downes 1979). They have also been found in planetary nebulae (Miranda et al. 2001), Mira variables (Hinkle & Barnes 1979), Asymptotic Giant Branch (AGB) stars (Barlow et al. 1996) and the centres of active galaxies (Claussen et al. 1984; Braatz, Wilson & Henkel 1996), but tend to be much fainter than in star-forming regions. Thus, HOPS will provide an untargetted survey of H_2O masers in star-forming regions over a substantial portion of our Galaxy. Comparison of the results of HOPS with the untargetted methanol multibeam survey (Cohen et al. 2007) will be useful in identifying the relative prevalence of the two maser species, as well as which stages of high mass star formation they are associated with. HOPS will also allow us to compare the relative occurrence of H_2O masers in regions of high and low mass star formation.

NH_3 is a tracer of dense quiescent gas. The (1,1) inversion transition typically exhibits prominent hyperfine structure, which can be used to infer the optical depth of the transition. Comparison of the (1,1) and higher J inversion transitions can be used to estimate the rotational temperature of the gas. A survey of NH_3 will trace the dense gas structure of our Galaxy, since it has an effective critical density of $\sim 10^5$ cm^{-3}. NH_3 is also known to occur in cold regions of gas, where more common gas tracers, like CO tend to deplete by freeze out onto dust grains (Bergin et al. 2006). This makes NH_3 a very useful tracer of the cold, dense regions of our Galaxy. The results of HOPS can be used to identify regions where the earliest stages of high mass star formation are taking place, as well as their broad physical properties such as average temperature, density and mass.

 10.1071/AS07053 1323-3580/08/02105

2 Observations

We used the Mopra Radiotelescope to map two one-square-degree regions located at Galactic longitudes of 305.5 and 333.2°. We centred each map slightly off the Galactic plane in order to assess how far off the Galactic plane we might find emission. Thus, the centres of the maps were (305.5°, +0.5°) and (333.2°, −0.7°). Adjacent scans were separated by 51 arcsec, to give nyquist sampling of the beam FWHM (2 arcmin) at the highest observing frequency (27.5 GHz). At lower frequencies, the observations consequently oversample the mapped region. The scanning rate was 15 arcsec s^{-1} and spectra were stored every 2 seconds, giving a 30-arcsec spacing between spectra in each row. The 2-second dump rate is the fastest that the telescope software can used, which limits the speed at which any map can be made. We could increase this speed by a factor of two so that the the data is dumped every half-beam, but prefer the slower speed to increase the signal to noise ratio. We mapped each region twice, scanning once in Galactic longitude and once in Galactic latitude and averaged each data cube. This method helps to reduce noise levels, as well as minimise artificial stripes that are introduced when only one scanning direction is used. It also allows us to carefully check spurious emission that may occur in one scan, but not the other. Each scan was completed in approximately 8 hours.

Observations were conducted in the first week of December 2006, during the Australian summer. We chose this time of the year partly to assess the effects of observing during summer. During the observations, the telescope was subjected to conditions ranging from hot, dry days, with temperatures rising as high as 310 K (37°C) to cool evenings, from clear skies to thin cloud cover to storms. We continued observations in all conditions except for storms to see how the data were affected.

The broadband mode of MOPS was used, with the frequency range covering between 19.5 and 27.5 GHz. Table 1 lists the brighter line transitions within this range. The channel width varied between 4.1 km s^{-1} at 19.5 GHz and 2.9 km s^{-1} at 27.5 GHz. This is usually insufficient to resolve Galactic thermal and maser lines as line widths are typically a few km s^{-1} or less.

Data were reduced using the ATNF dedicated packages 'LIVEDATA' and 'GRIDZILLA' developed by Mark Calabretta[1]. LIVEDATA performs a bandpass calibration for each row, using the preceding OFF scan. A 1st order polynomial (i.e. a straight line) is the fit to the baseline. GRIDZILLA regrids and combines the data from multiple scanning directions onto a data cube with pixels 30 × 30 arcsec. The data are also weighted according to the relevant T_{sys}.

3 Results

Data cubes were made for each of the lines listed in Table 1. Emission was detected in the H_2O, NH_3, radio recombination lines (H69α to H62α) and HC_3N data cubes. The integrated intensity map for NH_3 (1,1) is shown in Figure 1 for G305.5+0.5 as an example. The prominent horizontal and vertical stripes seen in the figure result from observations made in inclement weather. The vertical stripes are most prominent between Galactic longitudes of 305.4 to 305.7° and 305.9 to 306°. The horizontal stripes are most prominent around Galactic latitudes of +0.1, +0.28 and +0.53°. Unfortunately, the striping makes it difficult to distinguish real astrophysical emission in the integrated intensity map.

Bad weather introduces noise into each spectrum and affects all frequencies approximately equally. Thus, it is easy to distinguish real line emission from bad weather noise in a spectrum because the real emission is confined to a narrow frequency range, typically a few channels wide. However, the traditional integrated intensity display, shown in Figure 1, appears to be dominated by noisy

Table 1. Lines in the 19.5 to 27.5-GHz range

Line name	Frequency (GHz)	Pilot survey detection	Maser or thermal?[a]
H69α	19.591	Y	Thermal
CH_3OH (2_1–3_0)	19.967	N	Both (II)
H68α	20.462	Y	Thermal
NH_3 (8,6)	20.719	N	Both
NH_3 (9,7)	20.735	N	Thermal
C_6H (15/2–13/2)	20.792	N	Thermal
NH_3 (7,5)	20.804	N	Thermal
NH_3 (11,9)	21.071	N	Both
NH_3 (4,1)	21.134	N	Thermal
H67α	21.385	Y	Thermal
H_2O (6_1–5_2)	**22.235**	**Y**	**Maser**
CCS (2_1–1_0)	22.344	N	Thermal
H66α	22.364	Y	Thermal
HC_7N (20–19)	22.559	N	Thermal
NH_3 (2,1)	23.099	N	Thermal
CH_3OH (9_2–10_1)	23.121	N	Maser (II)
H65α	23.404	Y	Thermal
CH_3OH (10_1–9_2)	23.444	N	Thermal
NH_3 (1,1)	**23.694**	**Y**	**Thermal**
NH_3 (2,2)	**23.722**	**Y**	**Thermal**
NH_3 (3,3)	**23.870**	**Y**	**Both**
NH_3 (4,4)	24.139	N	Thermal
NH_3 (5,5)	24.533	N	Both
NH_3 (6,6)	25.056	N	Both
H64α	24.509	Y	Thermal
CH_3OH (3_2–3_1)	24.928	N	Both (I)
CH_3OH (4_2–4_1)	24.933	N	Both (I)
CH_3OH (2_2–2_1)	24.934	N	Both (I)
CH_3OH (5_2–5_1)	24.959	N	Both (I)
CH_3OH (6_2–6_1)	25.018	N	Both (I)
CH_3OH (7_2–7_1)	25.124	N	Both (I)
H63α	**25.686**	**Y**	**Thermal**
HC_5N (10–9)	26.626	N	Thermal
H62α	26.939	Y	Thermal
HC_3N (3–2)	**27.294**	**Y**	**Thermal**
CH_3OH (13_2–13_1)	27.472	N	Thermal
NH_3 (9,9)	27.477	N	Thermal

Lines marked in bold are the main target lines for HOPS.
[a]For CH_3OH masers, they are identified either as Class I or II

[1] http://www.atnf.csiro.au/people/mcalabre/livedata.html

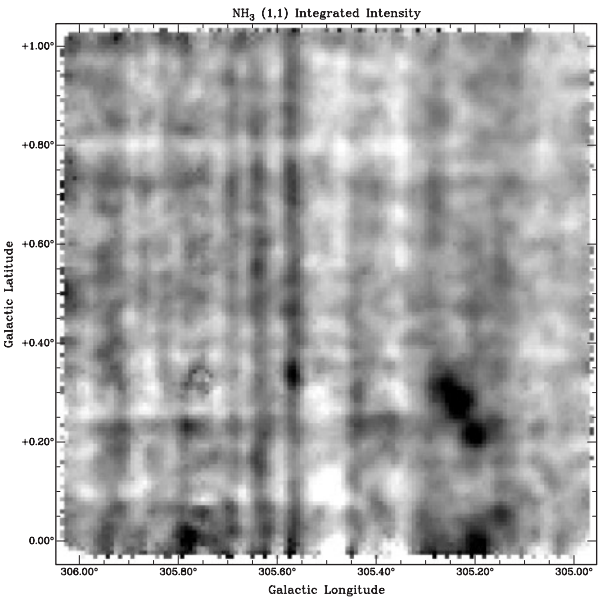

Figure 1 NH_3 (1,1) integrated intensity map for G305.5+0.5. Prominent horizontal and vertical stripes are the result of observing during bad weather. Real NH_3 emission can be seen around G305.2+0.25.

data: any real emission is confused with the noisy data. In order to minimise the visual impact of the striping, we employed a method that highlighted real emission over the artifacts introduced by bad weather. For each position-element in the data cube (effectively each pixel in the integrated intensity map) we calculated the RMS noise level and the peak intensity level of the spectrum at that postion. We then formed a new map where each element is the ratio of the peak intensity level to the RMS noise level. This effectively creates a map where the brightest pixels indicate real, narrow-lined emission and can therefore be used as an approximate guide to the morphology and extent of real emission in the data cube. Emission maps for G305.5+0.5 and G333.2−0.7 are shown in Figures 2 and 3, respectively. Note that because the brightness shown in these maps depends on a changing RMS noise level, the intensity cannot be used to reliably represent real emission intensity.

We remind the reader that this pilot survey is not designed to produce the best map of emission possible: that is left for the main HOPS. It is designed to determine what we can expect from the main survey. HOPS observations will not be made in such poor weather conditions.

3.1 G305.5+0.5

The H_2O maser emission map in Figure 2 shows four clear maser detections as black spots in a complex emitting region centred on G305.2+0.25. The '+' symbols in the map show all H_2O masers that were identified by careful inspection of the full data cube; a peak-intensity map was constructed using the peak pixel in each spectrum at every position in the map. Each pixel 5σ above the RMS noise level in this map was visually checked for real maser emission, as opposed to a noise spike. Real maser emission is distinguished by ocurring in more than one spectral channel and more than one spatial pixel. In this field we detect eleven H_2O masers, seven of which are new. The other emission maps shown in Figure 2 also show emission confined to the bottom right corner. Figure 4 shows spectra of emission in all detected lines from G305.2+0.2, which is circled in the H_2O maser map in Figure 2. A summary of detected emission towards each H_2O maser is given in Table 2. In Table 2 the first two columns denote the position of the H_2O masers in Galactic coordinates. The third column identifies each H_2O maser as a new or previous detection. New H_2O masers in G333.2−0.7 marked with an asterisk were observed but not detected by Breen et al. (2007), which is probably due to intrinsic variability of the masers. The remaining columns are either noted with a 'Y', indicating that emission was detected in the transition or a 'N', indicating no emission was detected at this position.

3.2 G333.2−0.7

Emission maps are shown in Figure 3. The H_2O maser emission map shows ten detected H_2O masers (plus symbols), five of which are new (see Table 2). Note that two of the detected masers appear to fall outside the mapped region. This is because the outer pixels in Figure 3 are automatically masked by the data processing routines when creating this emission map. The H_2O masers appearing outside this region were identified in the original H_2O maser data cube.

NH_3, HC_3N and H63α appear stronger and more extended than in Figure 2. Figure 5 shows spectra of detected emission at G333.14−0.44, represented by the circle in Figure 3. Again, all lines are clearly detected. The outer hyperfine components of NH_3 (1,1) can also be seen. A summary of detected emission towards each H_2O maser is given in Table 2.

Breen et al. (2007) conducted an untargetted survey of H_2O masers having a substantial overlap with our test region. We note that Breen et al. (2007) detected three masers (their sources 6, 7 and 8) that we did not detect. It is difficult to identify the reason for this as the broadband mode of HOPS has much wider channels (3.6 km s^{-1}) than Breen et al. (2007) (0.25 km s^{-1}), making a direct comparison of sensitivities dependant on the velocity structure of the emission. For example, with much broader channels, we are unlikely to detect a single, weak narrow-lined maser feature, but a maser site comprising of many weak individual maser peaks, closely spaced in velocity (within 3.6 km s^{-1}) is more likely to be detected by us. However, it is likely that maser variability plays a major part. Variablility is a likely explanation for the non-detection of source 6 in our pilot survey as this maser did not appear in followup observations by Breen et al. (2007). A more detailed comparison of previously detected masers and HOPS observations will be conducted during the main survey, when we use the narrowband mode and can directly compare narrow lined emission. Due to the inherent variability

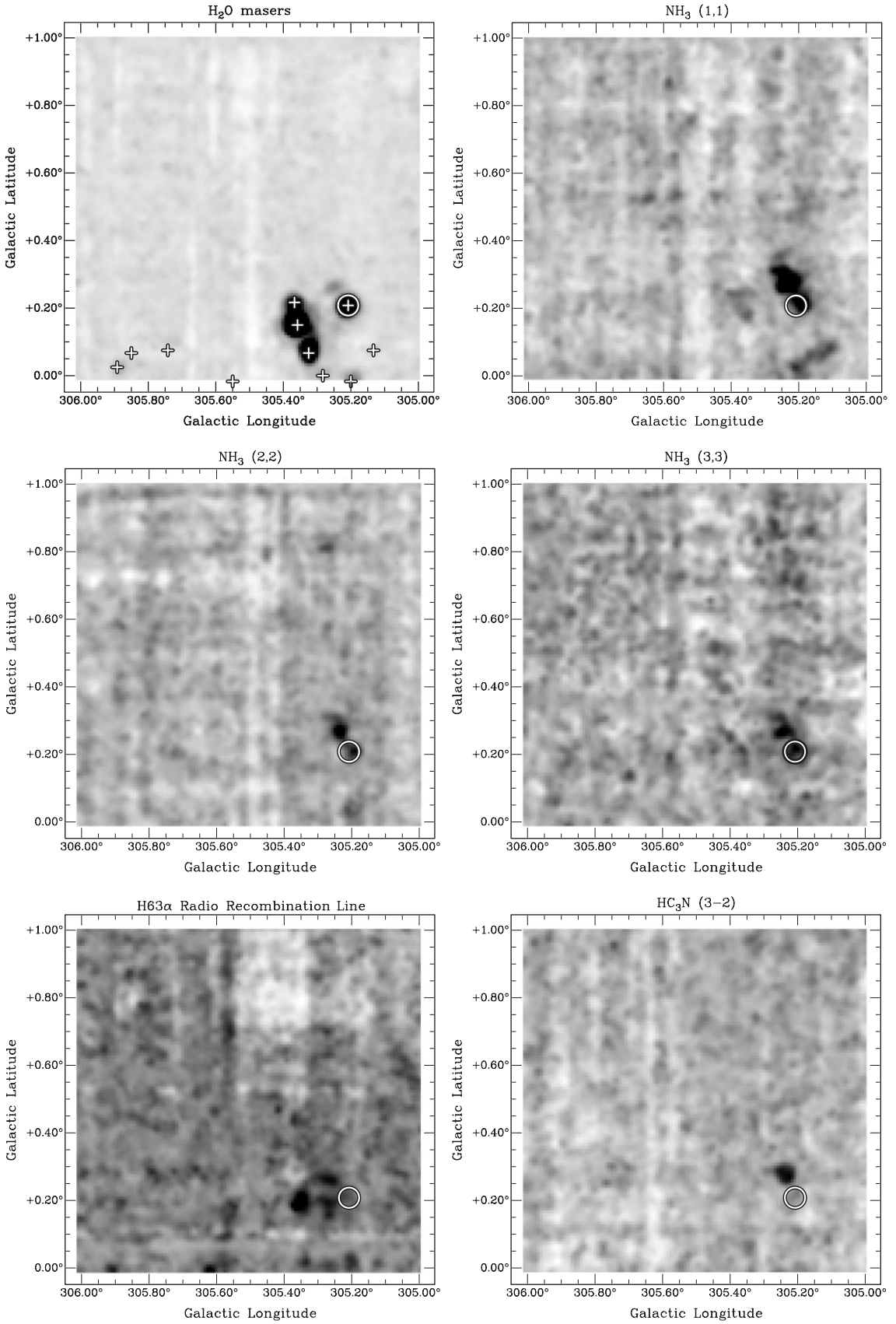

Figure 2 Peak intensity to noise ratio images for G305.5+0.5. These images show the ratio of the peak intensity to RMS noise level derived from the spectrum at each pixel. They show where real emission occurs and down-weight the contribution due to noisy data. Top-left is the image for H_2O masers, top-right is NH_3 (1,1), middle-left is NH_3 (2,2), middle-right is NH_3 (3,3), bottom-left is H63α radio recombination line and bottom-right is HC_3N (3–2). The + symbols on the H_2O maser image indicate the positions of detected H_2O masers. The circle on the H_2O maser image shows the position of spectra shown in Figure 4.

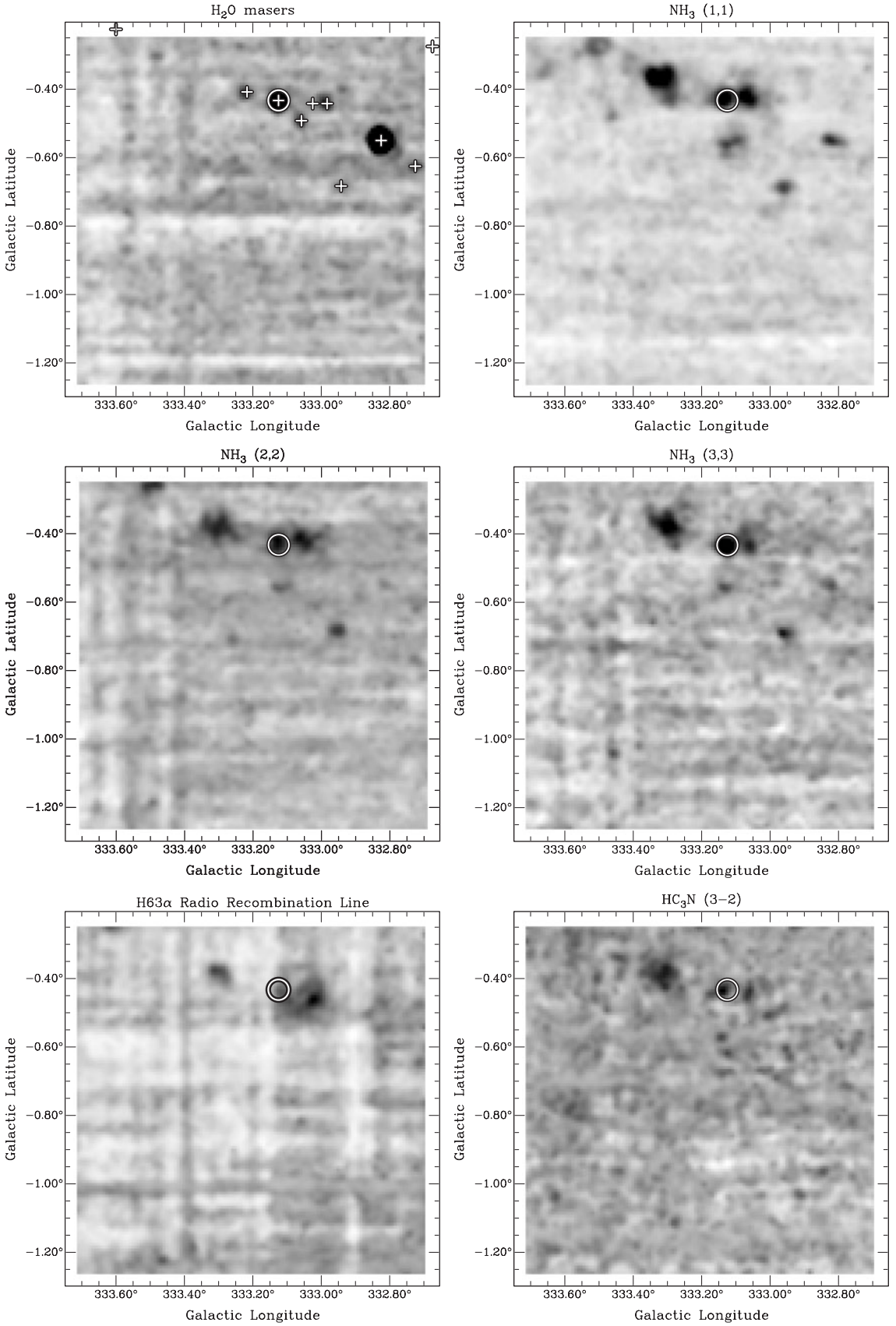

Figure 3 Peak intensity to noise ratio images for G333.2−0.7. These images show the ratio of the peak intensity to RMS noise level derived from the spectrum at each pixel. They show where real emission occurs and down-weight the contribution due to noisy data. Top-left is the image for H_2O masers, top-right is NH_3 (1,1), middle-left is NH_3 (2,2), middle-right is NH_3 (3,3), bottom-left is H63α radio recombination line and bottom-right is HC_3N (3–2). The + symbols on the H_2O maser image indicate the positions of detected H_2O masers. The circle on the H_2O maser image shows the position of spectra shown in Figure 5.

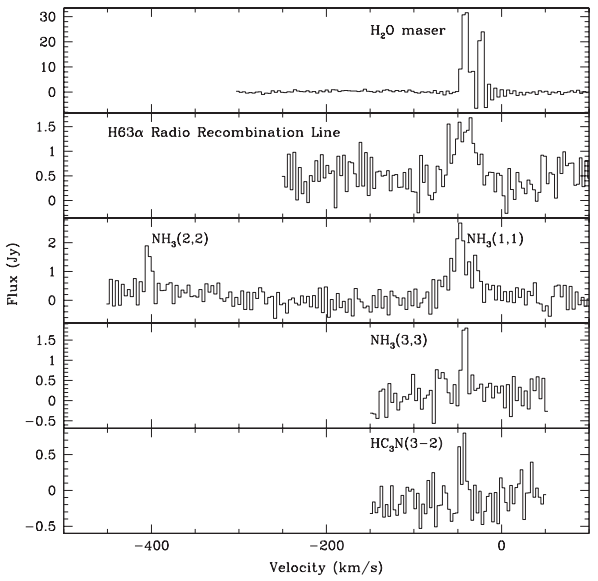

Figure 4 Spectra of detected emission lines at G305.20+0.20. From the top spectrum, running down the page: H_2O maser, H63α, NH_3 (1,1) and (2,2), NH_3 (3,3) and HC_3N (3–2). Note that all radio recombination lines from H69α to H62α were detected, but only H63α is shown here.

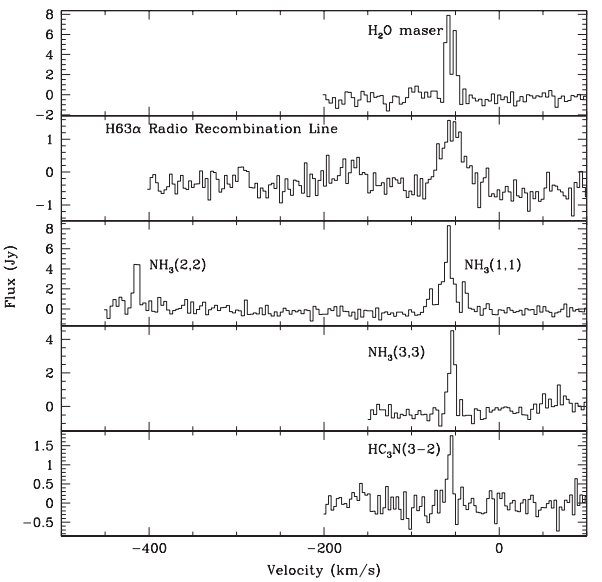

Figure 5 Spectra of detected emission lines at G333.14−0.44. From the top spectrum, running down the page: H_2O maser, H63α, NH_3 (1,1) and (2,2), NH_3 (3,3) and HC_3N (3–2). Note that all radio recombination lines from H69α to H62α were detected, but only H63α is shown here.

Table 2. Detections of other species at the positions of H_2O masers and previous H_2O maser identifications, for both G305.5+0.5 and G333.2−0.7

l (deg)	b (deg)	H_2O maser	NH_3 (1,1)	NH_3 (2,2)	NH_3 (3,3)	H63α (RRL)	HC_3N (3–2)
305.13	+0.08	New	Y	Y	N	N	N
305.20	−0.02	a	Y	Y	N	Y	Y
305.21	+0.21	b	Y	Y	Y	Y	Y
305.28	+0.00	New	Y	Y	N	Y	N
305.33	+0.07	New	N	N	N	Y	N
305.36	+0.15	c	Y	Y	N	Y	N
305.37	+0.22	d	Y	Y	Y	Y	N
305.55	−0.02	New	N	N	N	Y	N
305.74	+0.08	New	N	N	N	N	N
305.85	+0.07	New	N	N	N	N	N
305.89	+0.03	New	Y	Y	N	N	N
332.68	−0.28	New	N	N	N	N	N
332.73	−0.63	New*	Y	N	N	Y	N
332.83	−0.55	e	Y	Y	Y	Y	N
332.94	−0.68	New	Y	Y	Y	N	N
332.98	−0.44	New	Y	Y	Y	Y	N
333.03	−0.44	New*	Y	Y	Y	Y	N
333.06	−0.49	f	Y	Y	N	Y	Y
333.13	−0.43	c	Y	Y	Y	Y	Y
333.22	−0.41	f	Y	Y	Y	Y	Y
333.60	−0.23	d	N	N	N	Y	N

a, Caswell et al. (1989); b, Kaufmann et al. (1976); c, Caswell et al. (1974); d, Johnston et al. (1972); e, Braz & Scalise (1982); f, Breen et al. (2007).

of H_2O masers and because HOPS will be a single-epoch survey, we will not be able to detect all H_2O masers above the sensitivity limit, but HOPS will give us a snapshot of maser emission.

4 Discussion

4.1 Weather and Summer Observations

We intend to make observations for HOPS during the Australian summer, when demand for telescope time is limited because 3-mm observing is not possible. Very few mm-wave observing projects have been carried out outside of the traditional winter observing season. Thus, it is important that we understand how the data might be affected by typical summer weather conditions like high temperatures and cloud cover. During the observations, we encountered many varied conditions. Our experience indicates that high temperatures do not seriously affect the data quality when the sky is clear and the humidity is low. The data are seriously affected when thick cumulus clouds or rain occurs over the telescope, leading to the stripes seen in Figure 1.

A plot of the RMS noise values for a time series of observations is shown in Figure 6. During the first 0.5 hours, there was clear weather. Between approximately 0.5 and 1.0 hours there were cumulus clouds over the telescope followed by a period of mediocre weather (some clear sky and some cumulus cloud cover) up to 1.5 hours. After 1.5 hours, cumulus cloud cover increased until around 2.4 hours when there was rain over the telescope. The rain continued until about 3.0 hours. The cumulus clouds slowly dissipated after this until about 4.5 hours, after which the weather was mainly clear sky, with some cirrus cloud over the telescope. The effects of the cirrus clouds can be seen as minor increases in the RMS noise level of a factor of a few in the bottom plot of Figure 6.

During the times of cumulus cloud cover or rain, the RMS noise level dramatically increased over the baseline level by factors of up to 400. The RMS noise level was

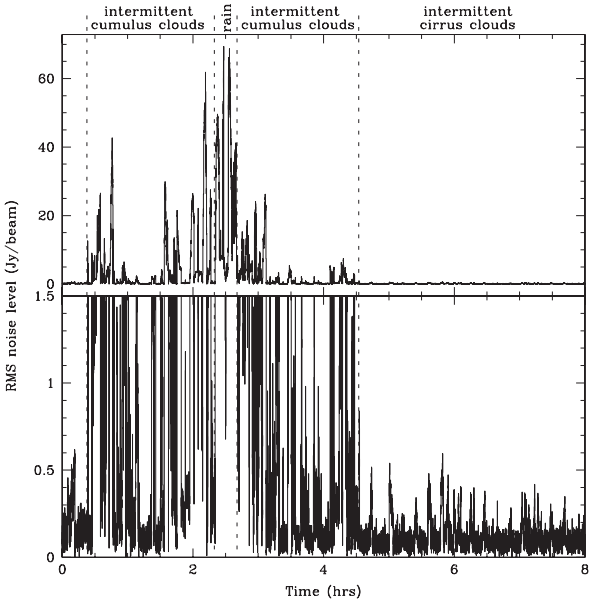

Figure 6 RMS noise levels calculated from spectra plotted as a function of time. The upper plot shows the full RMS noise range, whereas the lower plot shows the same RMS noise data scaled to show only the lowest noise data, below 1.5 Jy per beam. Above the plots are descriptions of the weather at various time periods separated by the dotted vertical lines.

below 0.4 Jy per beam (three times the baseline level) only 7% of the time. We consider these conditions to be bad weather. Note that the baseline or nominal good weather RMS noise level in Figure 6 is approximately 0.13 Jy per beam and can be seen after about 4.5 hours. During the time after 4.5 hours where there were only cirrus clouds or clear sky over the telescope the noise is below 0.4 Jy per beam (three times the baseline level) for 98% of the time. We consider these conditions to be good weather. Such a strong contrast in the RMS noise levels between good and bad weather make it easy to discern between the two.

We found that over the entire observing run the noise level is below 0.4 Jy per beam for 70% of the time. We also found that there was good weather (i.e. cirrus clouds or clear sky) approximately 70% of the time, during our time at the telescope, which included observations for other projects totalling one week. This figure takes into account observing both during the day and the night, however we observed that the cumulus clouds tend to form in the afternoons, with significantly less cumulus clouds during the night and early morning. We intend to take advantage of this by restricting observations to night and early morning. Thus, we assume that at least 70% of the observing time will be useful for HOPS, when only cirrus or clear sky is over the telescope. For times when the weather is not good enough for observations, we will flag out the bad data, re-observe this portion of the sky and substitute this for the bad data.

We note that the RMS noise levels quoted above are based on the H_2O maser data. We found that in comparison, the RMS noise levels do not change by more than 15% over these levels at different frequencies in the band.

4.2 H_2O Maser Detection Rate

Over the two fields covered, we detected a total of 21 masers, with 11 in G305.5+0.5 and 10 in G333.2−0.7. As detailed below, we expect to have better sensitivity to H_2O masers in the main HOPS. We therefore expect to detect more than 1000 masers over ninety square degrees of the Galactic plane, assuming at least 11 masers per square degree. Based on the number of new detections in the pilot survey (12), we may expect about half of the maser detections to be new, although we caution that this is based on a very small sample of detections.

4.3 Galactic-Latitude Distribution

In order to specify how wide in Galactic latitude HOPS should be, we investigated how far off the Galactic plane we can find emission. As can be seen from Figures 2 and 3, all the emission (both thermal and maser) is confined tightly to the Galactic plane and does not extend further than these maps. For G305.5+0.5, the emission is well confined within 0.5° of the Galactic plane. This is also true for nearly all of the emission seen in G333.2−0.7. Therefore, we define the HOPS width to be ±0.5° in Galactic latitude, which will allow us to observe most of the detectable thermal emission in our Galaxy using this setup. For cases like G333.2−0.7, where emission appears to extend beyond these limits, we will supplement the HOPS with maps to cover the extended emission.

Although H_2O and Class II methanol masers do not trace identical populations, there is a good deal of overlap between the two (e.g. Beuther et al. 2002). We can estimate the percentage of H_2O masers that might occur outside our survey region by assuming a similar Galactic latitude distribution as methanol masers. Walsh et al. (1997) targetted a large sample of *IRAS* sources and determined a FWHM distribution of 0.5° for methanol masers. This agrees with the distribution found in an untargetted, but smaller sample, survey of methanol masers by Pandian & Goldsmith (2007). Based on this, approximately 70% of methanol masers should occur within 0.5° of the Galactic plane. Therefore, we expect that about 30% of H_2O masers will lie outside the HOPS survey region.

We note that there is one weak source of NH_3 (1,1) emission detected in the G305.5+0.5 map far from the Galactic plane, located at G305.53+0.76. This will be discussed further in §4.5.

4.4 Detected Lines and Spectrometer Mode

The lines that were detected in this pilot survey are H_2O masers, NH_3 (1,1), (2,2) and (3,3), radio recombination lines H62α to H69α and HC_3N (3–2). Since the multiple radio recombination lines are largely redundant, we consider that we have detected six unique lines. As previously mentioned, these pilot observations were conducted using the broadband mode of MOPS, which covers the entire 8.4 GHz band, but yields only moderate velocity resolution of a few km s^{-1} per channel. We chose to observe in

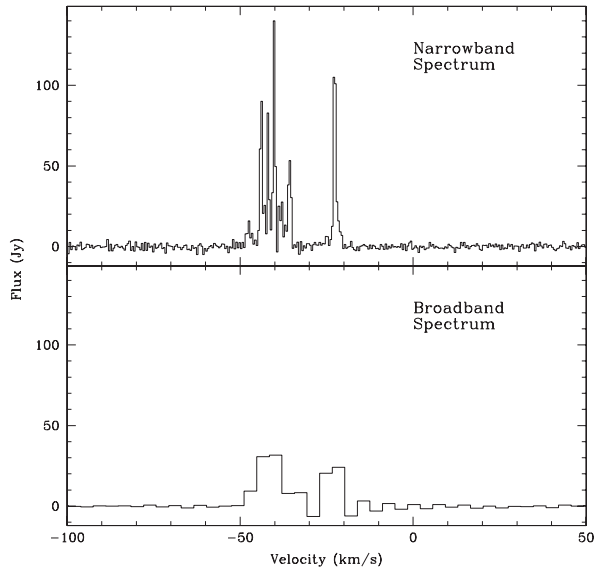

Figure 7 H_2O maser spectra for (top) narrowband zoom mode and (bottom) broadband mode plotted using the same scaling. The narrowband spectrum shows more detail in the emission features and allows the detection of weaker masers in the spectrum.

this mode because we did not know how many lines we might detect in this frequency range.

The MOPS has an alternate mode, called 'zoom' mode, in which up to sixteen 137.5 MHz-wide spectra can be taken simultaneously. These spectra are divided up into four sets of four spectra, with one set for each 2.2-GHz IF. Within each IF, there is virtually unlimited freedom to tune each of the four spectra. As noted above, we only detected six lines in the pilot survey, which can be adequately accommodated using the zoom mode. With 4096 channels per spectrum, we will have 0.5 km s^{-1} per channel resolution in HOPS. This has the added bonus of effectively increasing the signal to noise ratio for narrow-lined maser detections, which suffer from bandwidth smearing in the broadband observations. Smaller bandwidths will also aid us in sky subtraction and baselining.

We repeated a small map around G305.20+0.20, whose spectra are shown in Figure 4. The small map used exactly the same settings (e.g. on-the-fly speed, reference position) as the main G305.5+0.5 map, except that the zoom mode was used. Comparison spectra of the detected H_2O maser are shown in Figure 7. It is clear that the zoom mode allows the detection of more maser emission structure in the spectrum, and that the maser features are more prominent, making their detection easier.

Using the broadband mode, the weakest maser we detected is G305.13+0.08, which has a peak flux density of 2.4 Jy. This is approximately a 5σ detection at this position in the map and gives a guide as to the detection limit in these observations. Given typical line widths of maser emission (about 1 km s^{-1} or less), we expect to achieve a factor of 2–3 improvement in sensitivity with the zoom mode. Since thermal lines tend to be a few km s^{-1}, it is expected that we may get a marginal improvement in sensitivity in some regions with line widths 2–3 km s^{-1}, but no improvement for line widths of 3–5 km s^{-1}.

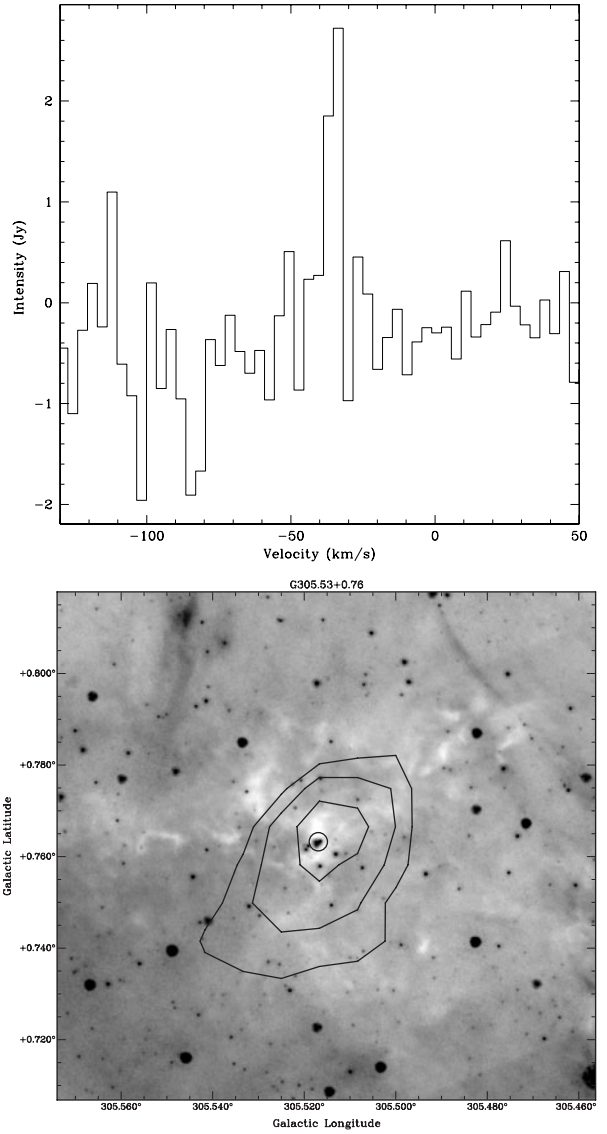

Figure 8 NH_3 (1,1) spectrum for G305.53+0.76 (top), showing emission at −34 km s^{-1}. Contours (bottom) show NH_3 (1,1) emission, superimposed on the greyscale which shows 8.0 μm emission from the GLIMPSE. An infrared dark cloud is seen to coincide with the peak of the NH_3 emission. The circle highlights an infrared source which shows unusually red colours, implying that it is deeply embedded.

4.5 G305.53+0.76: a New NH_3 Cloud

We detected a weak NH_3 (1,1) feature far removed from the bulk of NH_3 emission in the G305.5+0.5 map at G305.53+0.76. The emission is not obvious in Figure 2 because it lies close to a noisy part of the data cube. The spectrum of this source is shown in the top half of Figure 8. The bottom half shows the contours of NH_3 emission overlayed on 8.0-μm emission, shown as greyscale. The 8.0-μm emission was taken as part of GLIMPSE (The Galactic Legacy Infrared Mid-Plane Survey Extraordinaire) with the *Spitzer Space Telescope* (Benjamin et al.

2003). The GLIMPSE 8.0-μm image clearly shows an infrared dark cloud coincident with the peak of NH_3 emission. Such a dark cloud suggests that this is a site of star formation. This is supported by the fact that the star found in the darkest part of the cloud (circled in Figure 8) has very red colours, when compared to the other GLIMPSE bands. This is indicative of a deeply embedded object.

Based on the NH_3 integrated intensity (33 K km s^{-1}), we can estimate the mass of the cloud. Note that we have assumed a beam efficiency of 0.5 for Mopra at 12 mm, but this value is not well characterised, resulting in some uncertainty in the integrated intensity. There is a tentative (2.5σ) detection of NH_3 (2,2), which we have used to estimate the kinetic temperature. We determine the kinetic temperature from the rotational temperature, using the standard formulation for NH_3 (1,1) and (2,2) spectra (Ho & Townes 1983). The kinetic temperature has an upper limit of 22 K and so we use 22 K as an estimate of the temperature in determining the column density. To estimate the NH_3 column density, we use equations 1 and 2 of Walsh & Burton (2006). Here we assume the dipole moment for NH_3 is 4.9×10^{30} C m^{-1} (1.48 Debye). The derived NH_3 column density is 4.9×10^{19} m^{-2}.

Pillai et al. (2006) find an average abundance ratio of $\chi_{NH_3} = N(NH_3)/N(H_2) = 4 \times 10^{-8}$ for infrared dark clouds, and so we adopt this value here. We assume a distance of 2.5 kpc to G305.53+0.76 based on the near kinematic distance. We choose the near kinematic distance because the infrared dark cloud is seen in absorption against the Galactic background emission. However, we caution that we do not consider this a robust distance due to the inherent uncertainty in kinematic distances. Thus, we only derive an approximate mass for G305.53+0.76 of $200 M_\odot$; this mass could vary by a factor of a few, given the uncertainties that go into the assumptions of the various factors. This mass is much smaller than those found in giant molecular clouds where high mass stars are thought to form. It is not clear whether or not this region will form low mass or high mass or any stars, but is worthy of further investigation to determine its nature.

5 HOPS Survey Design

Having completed the pilot survey, we can now outline the main HOPS. We intend to survey the regions from $l = 300°$ through to $l = 0$ (the Galactic centre) and on to $l = 30°$. Galactic latitudes of $b = +0.5°$ to $b = -0.5°$ will be covered. This will result in a total of ninety square degrees surveyed. Therefore, we will concentrate on the busier regions of the inner Galaxy. We will observe the following lines as our main targets: H_2O masers, NH_3 (1,1), (2,2) and (3,3), H63α and HC_3N (3–2), using the zoom mode, which will allow us to detect weaker masers than in the pilot survey. Given these specifications, and that we have detected 21 masers in two square degrees, we expect to detect at least 1000 H_2O masers and a few hundred sources of each of the other tracers in HOPS. The spare zoom windows will be used to look for emission that may sporadically occur, such as non-metastable masing transitions of NH_3, Class I and Class II CH_3OH masers.

It is hoped that HOPS will yield a large sample of H_2O masers that can be directly compared to other masing species (e.g. 6.7-GHz CH_3OH Class II masers) with a statistically unbiased sample. In addition, the NH_3 emission can be used to map out the spiral structure of the southern Galaxy and tell us about the high-density structure of our Galaxy ($n > 10^5$ cm^{-3}). Such a high density survey can then be compared to lower density surveys using ^{12}CO ($n \sim 10^2$ cm^{-3}) (Mizuno et al. 2001).

Acknowledgments

We thank the Australian Research Council and UNSW, The University of Sydney and Monash University for funding to provide the UNSW MOPS spectrometer used for these observations. We thank the anonymous referee whose comments have greatly improved the quality of this paper.

References

Bains, I. et al., 2006, MNRAS, 367, 1609
Barlow, M. J. et al., 1996, A&A, 315, L241
Braatz, J. A., Wilson, A. S. & Henkel, C., 1996, ApJS, 106, 51
Braz, M. A. & Scalise, E., Jr., 1982, A&A, 107, 272
Benjamin, R. A. et al., 2003, PASP, 115, 953
Bergin, E. A., Maret, S., van der Tak, F. F. S., Alves, J., Carmody, S. M. & Lada, C. J., 2006, ApJ, 645, 369
Beuther, H., Walsh, A., Schilke, P., Sridharan, T. K., Menten, K. M. & Wyrowski, F., 2002, A&A, 390, 289
Breen, S. L. et al., 2007, MNRAS, 377, 491
Caswell, J. L., Batchelor, R. A., Forster, J. R. & Wellington, K. J., 1989, AuJPh, 42, 331
Caswell, J. L., Batchelor, R. A., Haynes, R. F. & Huchtmeier, W. K., 1974, AuJPh, 27, 417
Cohen, R. J. et al., 2007, in IAU Symposium 273, Triggered Star Formation in a Turbulent ISM, Eds. Elmegreen, B. G. & Palous, J. (Cambridge: Cambridge University Press), 403
Claussen, M. J. et al., 1984, ApJ, 285, L79
Genzel, R. & Downes, D., 1979, A&A, 72, 234
Hinkle, K. H. & Barnes, T. G., 1979, ApJ, 227, 923
Ho, P. T. P. & Townes, C. H., 1983, ARA&A, 21, 239
Johnston, K. J., Robinson, B. J., Caswell, J. L. & Batchelor, R. A., 1972, ApL, 10, 93
Kaufmann, P. et al., 1976, Natur, 260, 306
Pandian, J. & Goldsmith, P. F., 2007, ApJ, 669, 435
Pillai, T., Wyrowski, F., Carey, S. J. & Menten, K. M., 2006, A&A, 450, 569
Miranda, L. F., Gómez, Y., Anglada, G. & Torrelles, J. M., 2001, Natur, 414, 284
Mizuno, A. et al., 2001, PASJ, 53, 1071
Walsh, A. J. & Burton, M. G., 2006, MNRAS, 365, 321
Walsh, A. J., Hyland, A. R., Robinson, G. & Burton, M. G., 1997, MNRAS, 291, 261